


Metallic conductivity in Na-deficient structural domain walls in the spin-orbit Mott insulator Na_2IrO_3

Franziska A. Breitner,^{*} Julian Kaiser, Anton Jesche[✉], and Philipp Gegenwart^{✉†}

Experimental Physics VI, Center for Electronic Correlations and Magnetism, University of Augsburg, Universitätsstr. 1, 86159 Augsburg, Germany

 (Received 3 October 2023; revised 10 November 2023; accepted 28 November 2023; published 8 December 2023)

Honeycomb Na_2IrO_3 is a prototype spin-orbit Mott insulator and Kitaev magnet. We report a combined structural and electrical resistivity study of Na_2IrO_3 single crystals. Laue back-scattering diffraction indicates twinning with $\pm 120^\circ$ rotation around the c^* axis while scanning electron microscopy displays nanothin lines parallel to all three b -axis orientations of twin domains. Energy dispersive x-ray analysis line scans across such domain walls indicate no change of the Ir signal intensity, i.e., intact honeycomb layers, while the Na intensity is reduced down to $\sim 2/3$ of its original value at the domain walls, implying significant hole doping. Utilizing focused-ion-beam microsectioning, the temperature dependence of the electrical resistance of individual domain walls is studied. It demonstrates the tuning through the metal-insulator transition into a correlated-metal ground state by increasing hole doping.

DOI: [10.1103/PhysRevB.108.235130](https://doi.org/10.1103/PhysRevB.108.235130)

I. INTRODUCTION

Spin-orbit (SO) coupling describes the interaction between the spin and the orbital motion of electrons. In condensed matter composed of light elements, SO coupling is very weak and often neglected. However, for heavy atoms with high nuclear charge, a substantial magnetic field in the reference frame of moving electrons couples to their spins, and SO coupling is the driving source for novel quantum states, such as topologically protected conducting surface states in topological insulators (TIs) [1]. Established TIs, based on semiconductors with s - and p orbitals, are well described by the band theory of noninteracting electrons. For theory and experiment, various topological phases in highly correlated electron systems are challenging [2–5].

Iridates are promising in this respect: due to the large atomic mass of iridium ions, a strong SO coupling of order 0.4 eV has been found [6–8], reaching the typical size of the Coulomb repulsion for $5d$ electrons. For the $5d^5$ electrons of Ir^{4+} ions in an octahedral crystal electric field the strong SO coupling breaks the sixfold degeneracy of the t_{2g} states leading to filled $j_{\text{eff}} = 3/2$ and half-filled $j_{\text{eff}} = 1/2$ bands. Since the latter band is narrow, even a small Coulomb repulsion could then open a Mott gap leading to a $j_{\text{eff}} = 1/2$ SO Mott insulator. The corresponding wave function is different from that of ordinary $s = 1/2$ Mott insulators as it contains an equal mixture of xy , yz , and zx orbitals with mixed spin up and down states [6]. One of the wave function's components is purely complex. Thus, $5d$ electrons will acquire a complex phase upon hopping via oxygen p orbitals. The experimental proof for the complex $j_{\text{eff}} = 1/2$ SO Mott state has been

obtained by resonant inelastic x-ray scattering [9]. The complex transfer integral for the hopping could lead, in suitable crystal structures, to topologically nontrivial states. Such scenarios have been discussed for pyrochlore and honeycomb iridates [2,4,10]. The $j_{\text{eff}} = 1/2$ spins in Na_2IrO_3 also give rise to a bond-dependent magnetic exchange that can be described by an extended Kitaev model [11]. Though these moments display a zigzag antiferromagnetic order at ~ 15 K [12–14], there is clear evidence for the presence of a dominating Kitaev interaction [15–18] at elevated temperatures and excitation energy.

Tuning SO Mott insulators by charge carrier doping into the metallic state seems interesting and promising. It is motivated, for instance, by the analogy between the perovskite $j_{\text{eff}} = 1/2$ SO Mott insulator Sr_2IrO_4 and the isostructural $s = 1/2$ Mott insulator La_2CuO_4 parent compound for high- T_c superconductivity. While angle-resolved photoemission spectroscopy (ARPES) and scanning tunneling microscopy (STM) indeed recorded signatures of a pseudogap in electron-doped $(\text{Sr}_{1-x}\text{La}_x)_2\text{IrO}_4$ [19,20], a fully metallic or superconducting electrical resistance behavior has not yet been reported for doped or pressurized Sr_2IrO_4 . The $j_{\text{eff}} = 1/2$ SO Mott state in honeycomb Na_2IrO_3 has been confirmed by the analysis of resonant inelastic x-ray scattering spectra [21] with charge gap of 0.34 eV, determined by ARPES and optical conductivity [22]. While Shitade *et al.* treated Na_2IrO_3 in the weak correlation limit as layered quantum spin Hall insulator [10], it is now clear that strong correlations are needed to account for its magnetism [17] and the size of the charge gap [22]. In the absence of a clear hierarchy of the energy scales for SO coupling, Coulomb repulsion, one-electron hopping and trigonal crystal field splitting, the band structure of Na_2IrO_3 has been proposed to sensitively depend on small structural variations and quantum phase transitions, separating trivial normal, metallic, and topological phases as functions of

^{*}franziska.breitner@physik.uni-augsburg.de

[†]philipp.gegenwart@physik.uni-augsburg.de

hopping strength were proposed earlier [23]. Even the possibility of topological spin-triplet superconductivity in charge carrier doped honeycomb iridates was considered theoretically [24].

While the bulk electrical resistance of Na_2IrO_3 displays three-dimensional variable-range hopping of carriers localized by disorder [12,25,26], similar as in other iridates, different experiments suggested the possibility of enhancing the conductivity at the surface. An ARPES study reported an in-gap feature hinting at a metallic surface state [27] which was later attributed to dispersive states approaching the Fermi level in the Na terminated cleavage planes [28]. Indeed, atomic resolution STM found different Na-deficient surface reconstructions [29]. Careful analysis of tunneling spectra at differently reconstructed surfaces revealed defect states in the bulk gap, as well as a V-shaped bandgap closing that was associated to surface states [30]. A reduced and temperature independent electrical resistivity, measured under UHV conditions on a freshly cleaved crystal, was related to such a surface conductivity channel [30]. On the other hand, argon plasma etching the surface of Na_2IrO_3 crystals after cleaving in air revealed first-order density-wave-like transitions in the electrical resistance around ~ 220 K and a Fermi liquid behavior below 20 K [31].

Motivated by these hints at a high tunability of the electronic properties, we decided to perform a combined structural and electrical resistivity study on Na_2IrO_3 . We started with carefully searching for possible structural domains. Indeed, Laue backscattering diffraction indicates three different orientations of the honeycomb lattice with mutual $\pm 120^\circ$ rotations. Interestingly, these domain boundaries are seen as straight long white lines by scanning electron microscopy and feature a significant Na deficiency. Focused-ion-beam (FIB) microsectioning of the domain walls allowed us to study their electrical resistance behavior. We find a clear tendency that increasing Na deficiency reduces the resistance and finally induces a completely metallic state down to lowest temperatures, indicating that Na_2IrO_3 has been tuned locally across the metal-insulator transition by hole doping.

II. METHODS

High quality single crystals of Na_2IrO_3 of several mm diameter were grown via solid state reaction, as described in [12]. For Laue back-scattering measurements a Philips PW1830/40 x-ray generator with tungsten anode and Photonic Science detector were utilized. The diffraction patterns were recorded with voltages of 10, 15, and 20 kV and a current of 30 mA. An exposure time of ten minutes was deemed sufficient, as prolonged exposure did not yield significant improvement of the diffraction patterns for crystals of good quality. Attempts were made to further improve the quality of the measured Laue patterns by polishing or cleaving the samples. However, no significant improvement was achieved. Data analysis of the Laue patterns was performed using the Crystal Maker software Single Crystal as well as our own program which allows to consider additive overlap of reflections as well as reflections due to proximity to the characteristic wave lengths of tungsten. A scanning electron microscope (SEM), Merlin Gemini 2 from Zeiss, equipped with an energy

TABLE I. Structural parameters of Na_2IrO_3 obtained from single-crystal x-ray data at 300 K [13].

Atom	Site	x	y	z	$U(\text{\AA}^2)$
Ir	4g	0.5	0.167(1)	0	0.001(1)
Na1	2a	0	0	0	0.001(6)
Na2	2d	0.5	0	0.5	0.009(7)
Na3	4h	0.5	0.340(2)	0.5	0.009(6)
O1	8j	0.748(6)	0.178(2)	0.789(6)	0.001(6)
O2	4i	0.711(7)	0	0.204(7)	0.001(7)

dispersive x-ray analysis (EDX) probe with X-Max 80N SDD detector from Oxford Instruments was utilized for structural and compositional investigation of cleaved Na_2IrO_3 surfaces. Silver epoxy was used to mount the crystals onto the sample holder. The dual beam FIB-SEM Crossbeam 550 from Zeiss was used for microstructuring and electrically contacting small surface areas for electrical resistivity measurements. The measurements were performed between 2 and 300 K in the Dynacool PPMS with ETO option from Quantum Design. All measurements were done with an excitation current of $3 \cdot 10^{-5}$ mA.

III. RESULTS AND DISCUSSION

A. Structural domains in Na_2IrO_3

As the crystal structure is relevant for the following discussion of our Laue data, we start with a brief overview. Na_2IrO_3 crystallizes in a monoclinic $C2/m$ structure with one Ir and three Na positions which are listed in Table I. The lattice constants are $a = 5.427(1)$ \AA , $b = 9.395(1)$ \AA , and $c = 5.614(1)$ \AA [12,32]. Due to its layered structure, which can be seen in Fig. 1(a), consisting of alternating Na and NaIr_2O_6 layers, Na_2IrO_3 is prone to stacking faults. Within the ab plane, as shown in Fig. 1(b), the Iridium atoms form a honeycomb structure where each Ir atom is surrounded by six oxygen atoms in an octahedral configuration and each honeycomb is filled by one Na atom.

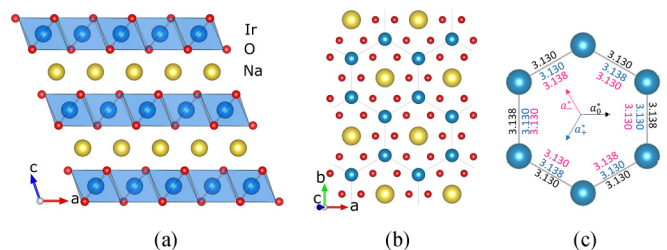


FIG. 1. Crystal structure of Na_2IrO_3 . Na atoms are colored yellow, Ir atoms blue, and O atoms red. (a) shows the layered structure perpendicular to the c axis which consists of alternating Na and NaIr_2O_6 layers. The honeycomb structure within the ab plane is depicted in (b). (c) depicts the honeycomb structure for three orientations differing by rotation of $\pm 120^\circ$ a_0^* (black), a_+^* (blue), and a_-^* (magenta). Due to the slight difference in Ir-Ir distances (given in \AA [13]), there is no perfect overlap of the Ir atoms for the three orientations.

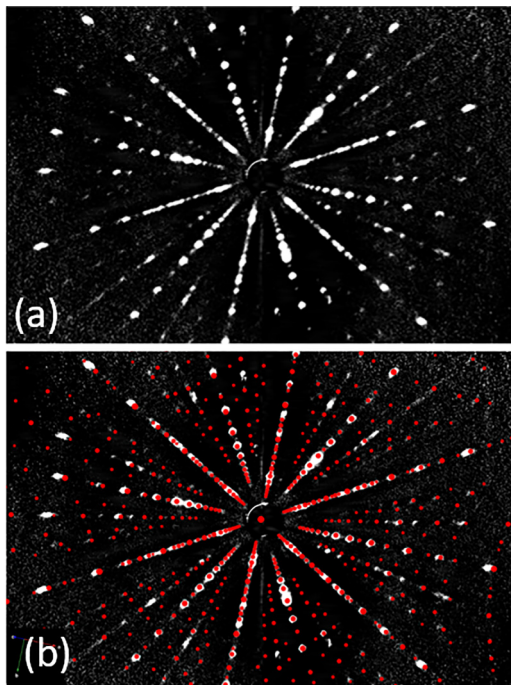


FIG. 2. (a) Laue pattern of Na_2IrO_3 recorded with an acceleration voltage of 20 kV after background subtraction. (b) The simulated pattern is shown for one of three possible orientations (a_0^*).

Na_2IrO_3 crystals grow as thin platelets with the c^* axis perpendicular to the a - b -plane surface. The honeycomb structure displayed in Fig. 1(c) has almost perfect threefold rotational symmetry around the c^* axis. It is slightly distorted due to trigonal distortions of the individual IrO_6 octahedra which change the Ir-O-Ir bond angles from the ideal value of 90° to somewhere in the range of 98 - 99.4° [13]. This results in a variation of the Ir-Ir distances ranging from 3.130 to 3.138 Å.

Figure 2(a) displays a representative measured Laue pattern of one of our crystals. After background subtraction, it is first analyzed using the simulation program Single Crystal. The pattern matches reasonably well with all three different

orientations with mutual $\pm 120^\circ$ rotations around the c^* axis, one being displayed in panel (b). These three orientations shall from now on be referred to as a_0^* (0°), a_+^* (rotation of $+120^\circ$), and a_-^* (rotation of -120°). Thus, at first glance, there appears to be no obvious preferred orientation.

Taking a closer look at reflections 1–6 depicted in Fig. 3(a), it becomes apparent that not all reflections can be described by the simulation of just one of the three orientations shown in Fig. 3(b). Here, neither reflection 5 nor 6 is matched by the simulation. One possible explanation for this would be that the detector sensitivity was underestimated. Indeed, a higher sensitivity yields a match for all observed reflections, as shown in Fig. 3(c), where the previously unexplained reflections can now be indexed as $\bar{6}2\bar{1}3$ and $\bar{6}2\bar{1}\bar{3}$. However, several additional reflections appear in the simulation, many of which are not detectable in the recorded Laue pattern. Furthermore, while the simulated reflections disappear for a lower acceleration voltage of 15 kV, both reflections 5 and 6 remain visible in the corresponding Laue pattern [see Fig. 3(d)]. Thus, another explanation is needed.

Rotating the honeycomb around 120° in either direction [blue or magenta in Fig. 1(c)] leads in some of the overlapping Ir-Ir-bonds to a mismatch in length. Looking at the individual Laue patterns for all three directions, this distortion results in most simulated reflections along (h 0 l) overlapping for a_0^* , a_+^* , and a_-^* . However, this is not the case for the (0 k l) direction. This leads to clearly visible reflections along (h 0 l) whereas those for (0 k l) appear smeared. Reflections where a_0^* , a_+^* , and a_-^* overlap would show comparatively higher intensities than expected if only one orientation would be present. Indeed, the simultaneous existence of a_0^* , a_+^* , and a_-^* offers the best match for the recorded data so far as can be seen in Fig. 3(e). Here, reflection 5 is explained by the $2\bar{4}\bar{8}$ reflection of a_+^* , and reflection 6 by the $2\bar{4}\bar{8}$ reflection of a_-^* . For signature 1 the reflections for all directions overlap, which explains the increased brightness of this reflection.

Looking again at reflections $\bar{3}1\bar{6}$, $\bar{3}1\bar{6}$, $\bar{2}4\bar{8}$, and $24\bar{8}$, we find all of them disappear for an acceleration voltage of 10 kV (not displayed). For 15 kV, however, the reflections are still detectable. The wave length of these reflections is close to that

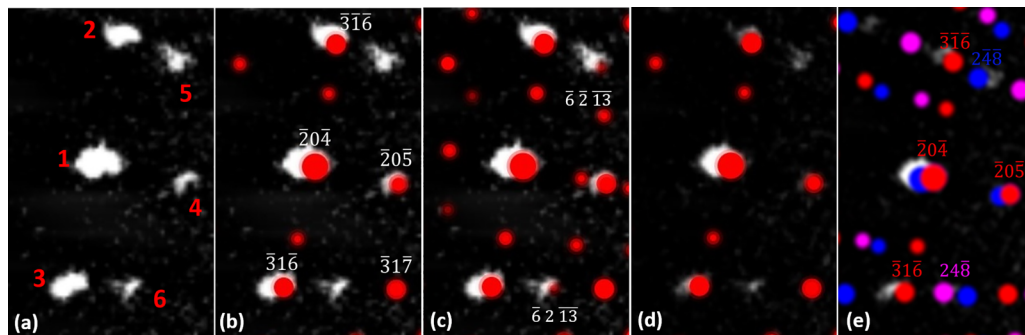


FIG. 3. Zoomed-in section of the previously depicted Laue pattern recorded at 20 kV (a). The relevant reflections are labeled 1–6 in order to be able to distinguish them in the following discussion. (b) shows the simulated reflections (red dots) for one direction (a_0^*), (c) shows those for a simulation with higher detector sensitivity. Here, all detected reflections can be matched, but the simulation also shows several additional signatures which were not detected in the measurement. (d) is the Laue pattern recorded at 15 kV along with the corresponding simulation. Both reflections 5 and 6 are still visible in the measurement yet have disappeared in the simulation. The simulation for simultaneous directions a_0^* , a_+^* , and a_-^* (red, blue, and magenta) in (e) shows a match for all reflections.

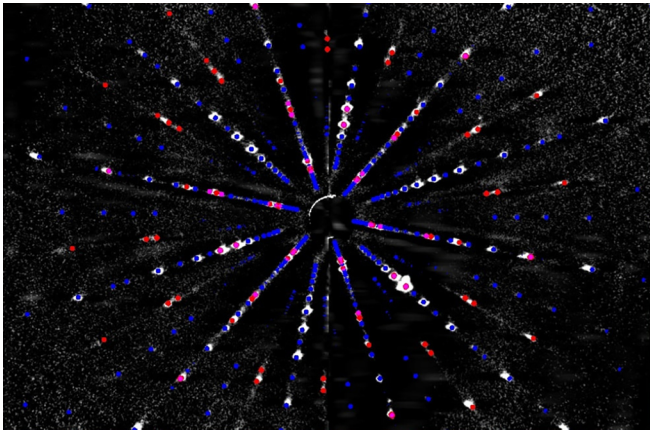


FIG. 4. Simulation of the Laue pattern of Na_2IrO_3 showing reflections visible due to additive overlap in blue, due to proximity to the characteristic lines of tungsten in red, and reflections where both occur in magenta. The simulation data was adjusted separately for both detector halves to allow for an optimal result.

for the L_{β_1} and L_{β_2} characteristic lines of tungsten [33] which can be detected for voltages above 12.1 kV (L_I absorption edge) and thus are absent at lower voltages.

Furthermore, as the intensity for the characteristic lines is far higher than that of the bremsstrahlung spectrum, reflections in the immediate vicinity of those lines might also be visible, while other reflections disappear in the background noise.

As the software Single Crystal does not have the capacity for pattern simulation taking into account the above mentioned issues, a self written program considering the characteristic lines as well as the additive overlap of individual reflections was utilized for simulation of such a Laue pattern. Here, we assume a direct proportionality of the intensity to the area of the reflections. Only the characteristic lines for L_{α_1} , L_{β_1} , and L_{β_2} are taken into consideration, as we found those to be the only ones significantly contributing to the diffraction pattern. Furthermore, only those reflections for which the wave length deviates less than $\Delta\lambda = 0.02 \text{ \AA}$ were assigned to the characteristic lines. Looking at the resulting Laue pattern, shown in Fig. 4, where both additive overlap and proximity to the characteristic lines of tungsten are taken into consideration for the simulation, we find this to be a good match for all detected reflections. Additionally, here the analysis was done separately for both detector halves in order to correct the slight mismatch of both pattern halves stemming from the detector halves not being aligned perfectly.

For Li_2IrO_3 , another member of the honeycomb iridates, stacking faults are attributed to occasional in-plane shifts of the layers by $\pm\bar{b}/3$ [13,34]. While, however, for a domain containing only a small number of layers, a rotation by 120° yields results similar to those for a translation by $\pm\bar{b}/3$; for larger domains the results for translation and rotation deviate. Thus, to the best of our knowledge, attributing the Laue reflections to the simultaneous presence of three crystal orientations with 120° rotation offers the best explanation, not only explaining the position of reflections but also the increased brightness of some reflections as well as the smearing of those reflections attributed to the $(0\ k\ l)$ direction.

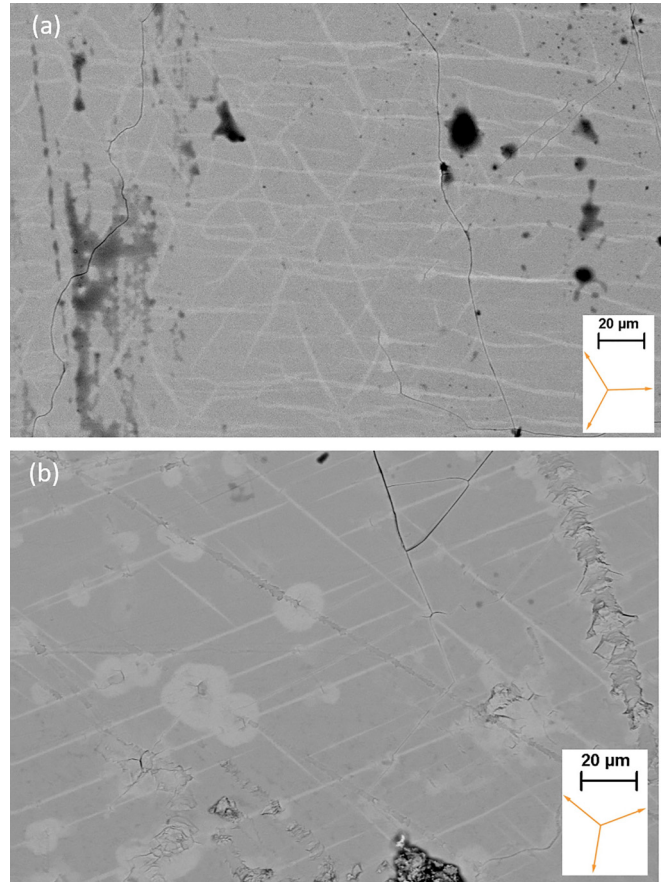


FIG. 5. SEM image of the surface of two samples of Na_2IrO_3 recorded using a material contrast sensitive detector. The insets on the right show the orientation of the b axes. While sample 5 (a) shows a more disordered arrangement, the lines in sample 4 (b) are straight and parallel. Despite these obvious differences, the Na deficient lines appear to be roughly oriented along the b axes, determined by Laue analysis for both samples. As Laue measurements were performed before EDX, the depicted samples have been exposed to air for several hours at this point. The dark spots in (a) as well as the bright dots in (b) are likely due to some contamination on the surface or small cracks which can create charging effects appearing bright in the image. This was also observed on other samples previously exposed to air, but is not found on fresh surfaces.

B. Imaging domain walls by EDX

SEM images recorded using a material contrast sensitive NTS-BS (Nano Technology Systems-Backscattered Electrons) detector show a series of brighter lines on the surface with a width in the range of up to $2 \mu\text{m}$, as shown in Fig. 5. These lines can be observed on untreated or polished crystals as well as on freshly cleaved surfaces and could also be found using other detectors, such as HE-SE2 (high efficiency secondary electron) or AsB (angular selective backscattered electron), where they appeared, however, far less prominent. While some of the lines are arranged parallel to each other, others are rotated by either 60° or 120° . Comparing the lines to the orientation of the crystal previously determined by Laue, many lines seem to be running along at least one of the three b axes. While some samples show more irregularly distributed

TABLE II. Na/Ir ratio determined by EDX for several samples at the detected lines and on the surrounding area (s).

Sample	$(\text{Na}/\text{Ir})_{\text{line}}$	$(\text{Na}/\text{Ir})_s$
1	1.5(2)	1.8(1)
2	1.5(2)	1.8(1)
3	1.3(1)	1.8(1)
4	1.3(1)	1.7(1)
5	1.2(2)	1.6(2)
6	1.1(2)	1.6(2)

and overall less straight lines, a rough assignment to the b axes remains possible for all investigated crystals for at least one direction. Through thorough investigation of the surface, we exclude topographical features such as steps, cracks or depositions as the origin of these lines. Combining SEM and Laue data we thus propose to assign these lines to structural domain walls separating differently oriented domains of Na_2IrO_3 . Note that in case of $(\text{Na}_{1-x}\text{Li}_x)_2\text{IrO}_3$ for $x > 0.25$ in the phase separated regime, line structures were also found in EDX, which however, can be associated with Li_2IrO_3 [35].

Figure 6 shows an enlarged image of these lines along with elemental distribution maps for sodium. Here green areas show a lower Na concentration compared to red ones. A linescan taken perpendicular to one of the lines clearly shows a dip in Na concentration which coincides with the brighter region in the SEM image.

STM measurements previously showed Na_2IrO_3 to be Na deficient on the surface with up to $2/3$ of the Na atoms missing [29]. However, this method is limited to the surface, whereas EDX can probe a volume of several hundred nanometers into the crystal [36]. All EDX data was recorded using a voltage of 20 keV. Table II summarizes the Na to Ir intensity ratios on the lines (i.e. on the domain walls), as well as the surrounding area for 6 different samples. First, we note that even away from the lines the ratio differs from the stoichiometric value of two. A reduction of the intensity ratio below two even away from domain boundaries on freshly cleaved samples likely points to the occurrence of reabsorption of the heavy Iridium atoms during EDX. Therefore, the intensity ratio does not directly equal the atomic ratio, though it is a measure of it. Clearly it is drastically reduced on the lines compared to the surrounding regions. The Na deficiency effectively hole dopes the iridate layers, whose impact on electrical transport is addressed below.

The lower Na concentration along the structural domain walls also explains their bright appearance in the SEM image, as within them the average atomic number is increased. It is not yet clear how deep into the crystal the lines penetrate. The fact that upon cleaving a crystal, lines could instantly be found on the fresh surfaces implies either an instantaneous formation upon exposition or a penetration depth reaching far into the crystal.

C. Electrical resistivity of domain walls

In order to study the electrical resistance of Na-deficient structural domain walls, FIB-assisted microsectioning and electrical contacting was utilized. Crystals were glued onto

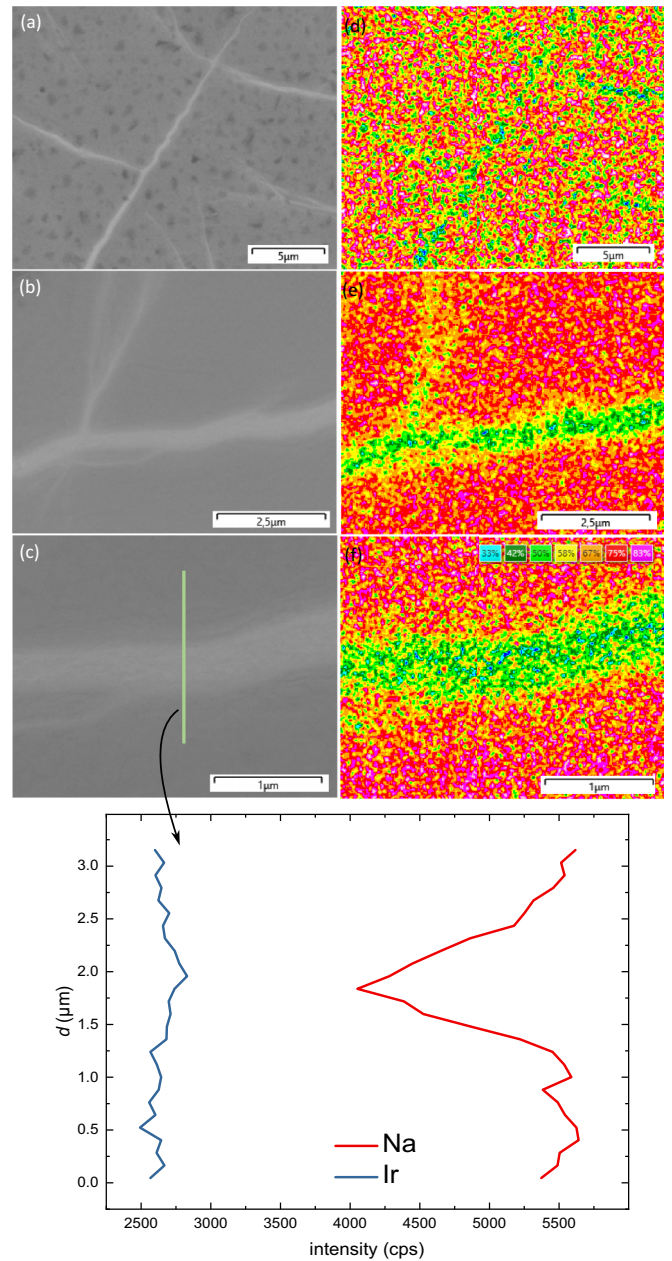


FIG. 6. Elemental distribution of Na determined via EDX for a single line using different magnifications on sample 1. The mapping clearly shows the occurrence of Na deficiency in the lines appearing bright in the SEM image. Here green areas indicate a Na percentage which is diminished compared to the red areas. A line scan of (c) is depicted on the right side to give a quantification of the Na deficiency.

sapphire substrates using epoxy resin, cleaved inside an argon filled glovebox, transferred to a sputter chamber without air exposure, and partially coated with gold. The samples were then structured using a FIB-SEM in a way that allowed for a four probe measurement along a defined area by contacting a line using gas-injection system (GIS) deposited Pt within the FIB chamber and cutting trenches to define the desired geometry [37], as can be seen in the inset of Fig. 7. Contacting was done in the same way for all depicted samples. Air contact of the gold covered sample surface was limited to

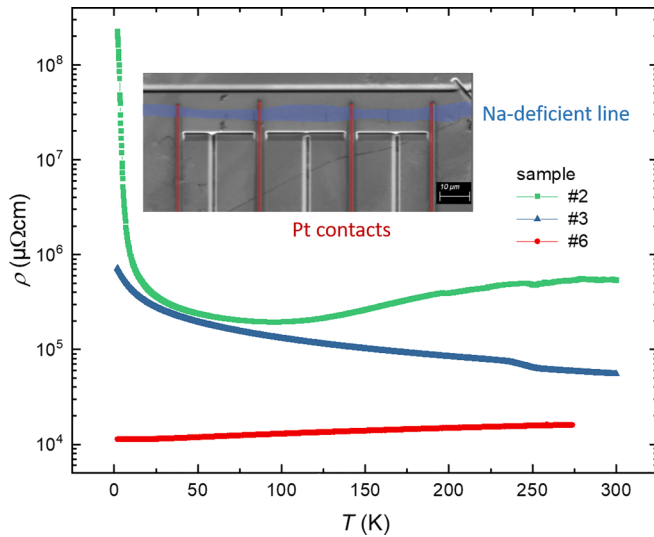


FIG. 7. Temperature dependence of the electrical transport of Na deficient lines on the surface of Na_2IrO_3 crystals with varying Na content. Decreasing Na concentration lowers the resistance due to hole doping. The sample with lowest Na content is completely metallic (red line). The inset shows a microstructure prepared and electrically contacted by FIB.

the transfer from the sputter chamber to the FIB. EDX was used to determine the Na-Ir ratio along the lines compared to the surrounding surface. Resistivity data for three such lines, each of which was recorded on a different crystal, can be seen in Fig. 7.

The absolute resistance was scaled with the geometrical parameters, such as the width of the lines from SEM, the distance of the voltage contacts, as well as the total sample thickness, to obtain the resistivity. This gives us an upper bound of the resistivity, since less Na deficiency in the inner parts, deeper below the surface, may reduce the effective thickness of the conducting regions. While absolute values are already rather small compared to previous measurements, we observe a further decrease for lower Na content of the lines. Sample 6 shows metallic behavior ($d\rho/dT > 0$) down to lowest temperatures. To check whether the metallic behavior is preserved over time, we remeasured the electrical resistance of sample 6 two subsequent times after air exposure. Prolonged contact with CO_2 and H_2O is known to lead to sample degradation [38]. As shown in Fig. 8, after two days of exposure to air, the resistivity still appeared metallic, yet the absolute values increased. After five days the resistivity shows entirely insulating behavior. The metallic behavior of sample 6 before air exposure cannot be explained by degradation, which by contrast enhances the resistivity. Instead, the metallic resistance indicates that the metal-insulator transition has been passed for Na deficient, i.e., hole-doped, Na_2IrO_3 .

Finally, we analyze the low-temperature data, cf. Fig. 9. The temperature dependence can be described using a sum of the residual resistance, electron-electron and electron-phonon scattering contributions according to $\rho = \rho_0 + aT^2 + bT^5$ [39]. The fitted coefficient $a = 0.062 \mu\Omega\text{cm}/\text{K}^2$ lies in between values for bilayer strontium iridate Sr_2RuO_4 along the c - and a axis and it is comparable to values for moderately

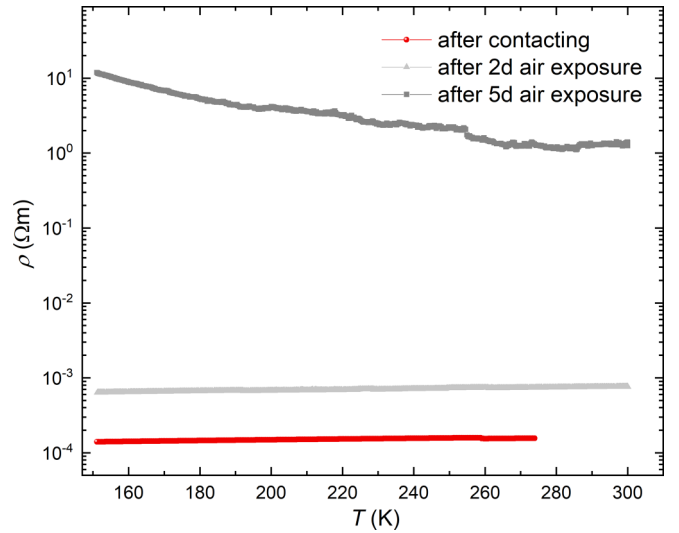


FIG. 8. Temperature dependence of the electrical resistance along a structural domain wall in sample 6 measured directly after contacting (red curve, from Fig. 7), as well as after two days (light gray) and five days (gray) of air exposure.

heavy $4f$ and $5f$ Kondo systems [40]. But of course this relies on the above assumption of a homogeneous Na deficiency across the entire sample thickness of ~ 20 – $40 \mu\text{m}$.

IV. CONCLUSION

In conclusion, Laue patterns of Na_2IrO_3 indicate structural domains and are perfectly well described by additive overlap of reflections from three different structural twins with 120° rotated b axes around the c^* axis. Complementary scanning electron microscopy (SEM) energy dispersive x-ray analysis on cleaved crystal surfaces revealed lines roughly along the

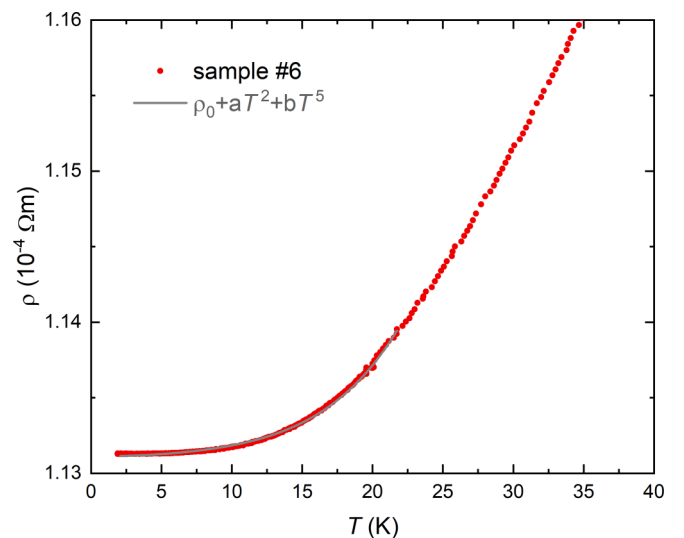


FIG. 9. Low temperature electrical resistivity along a structural domain wall in sample 6. The solid line represents correlated metallic behavior according to $\rho(T) = \rho_0 + aT^2 + bT^5$ with $\rho_0 = 1.13 \cdot 10^4 \mu\Omega\text{cm}$, $a = 6.18 \cdot 10^{-2} \mu\Omega\text{cm}/\text{K}^2$, and $b = 1.11 \cdot 10^{-5} \mu\Omega\text{cm}/\text{K}^5$.

different b axes with significant (up to $1/3$) Na deficiency compared to the surrounding areas. We thus associate these lines to structural domain walls. Resistivity measurements along individual domain walls in FIB-assisted microstructured samples reveal a dependence of the resistance on their Na to Ir ratio, with lower Na content and thus, increased hole doping corresponding to lower resistivity. For the domain wall with highest Na deficiency, a completely metallic behavior down to 2 K has been found, indicating that Na_2IrO_3 can be tuned locally across the metal-insulator transition. The observed coefficient of T^2 resistivity behavior suggests a moderately correlated metal state, though the absolute values of the resistance are governed by the uncertainty of the effective thickness of the domain boundaries.

At first glance, this behavior reminds to conductive domain walls observed in other otherwise insulating materials, such as

ferroelectrics [41–43], where conductivity can be tuned by the application of an electric field. This leads to non-Ohmic I-V characteristics which have also been observed for Na_2IrO_3 [26,30]. However, in the case of Na_2IrO_3 it is known from ARPES measurements that Na deficiency or additional deposited Na atoms influence the charge carrier density, and thus the Fermi level [26–28], and our analysis reveals a clear Na deficiency at the domain walls, which is thus at the origin of the conducting behavior.

ACKNOWLEDGMENTS

Technical support by Klaus Wiedenmann is gratefully acknowledged. We thank Dr. Toni Helm for advice regarding the FIB preparation of samples. This work was supported by the German Research Foundation project 492547816 (TRR 360).

-
- [1] J. E. Moore, The birth of topological insulators, *Nature (London)* **464**, 194 (2010).
- [2] D. Pesin and L. Balents, Mott physics and band topology in materials with strong spin-orbit interaction, *Nat. Phys.* **6**, 376 (2010).
- [3] M. Dzero, K. Sun, V. Galitski, and P. Coleman, Topological Kondo insulators, *Phys. Rev. Lett.* **104**, 106408 (2010).
- [4] J. G. Rau, E. K.-H. Lee, and H.-Y. Kee, Topological Kondo insulators, *Annu. Rev. Condens. Matter Phys.* **7**, 195 (2016).
- [5] Y. Tokura, Quantum materials at the crossroads of strong correlation and topology, *Nat. Mater.* **21**, 971 (2022).
- [6] B. J. Kim, H. Jin, S. J. Moon, J.-Y. Kim, B.-G. Park, C. S. Leem, J. Yu, T. W. Noh, C. Kim, S.-J. Oh, J.-H. Park, V. Durairaj, G. Cao, and E. Rotenberg, Novel $J_{\text{eff}} = 1/2$ mott state induced by relativistic spin-orbit coupling in Sr_2IrO_4 , *Phys. Rev. Lett.* **101**, 076402 (2008).
- [7] H. Watanabe, T. Shirakawa, and S. Yunoki, Microscopic study of a spin-orbit-induced mott insulator in Ir oxides, *Phys. Rev. Lett.* **105**, 216410 (2010).
- [8] J. P. Clancy, N. Chen, C. Y. Kim, W. F. Chen, K. W. Plumb, B. C. Jeon, T. W. Noh, and Y.-J. Kim, Spin-orbit coupling in iridium-based $5d$ compounds probed by x-ray absorption spectroscopy, *Phys. Rev. B* **86**, 195131 (2012).
- [9] B. Kim, H. Ohsumi, T. Komesu, S. Sakai, T. Morita, H. Takagi, and T.-h. Arima, Phase-sensitive observation of a spin-orbital Mott state in Sr_2IrO_4 , *Science* **323**, 1329 (2009).
- [10] A. Shitade, H. Katsura, J. Kuneš, X.-L. Qi, S.-C. Zhang, and N. Nagaosa, Quantum spin hall effect in a transition metal oxide Na_2IrO_3 , *Phys. Rev. Lett.* **102**, 256403 (2009).
- [11] J. Chaloupka, G. Jackeli, and G. Khaliullin, Kitaev-heisenberg model on a honeycomb lattice: Possible exotic phases in iridium oxides A_2IrO_3 , *Phys. Rev. Lett.* **105**, 027204 (2010).
- [12] Y. Singh and P. Gegenwart, Antiferromagnetic Mott insulating state in single crystals of the honeycomb lattice material Na_2IrO_3 , *Phys. Rev. B* **82**, 064412 (2010).
- [13] S. K. Choi, R. Coldea, A. N. Kolmogorov, T. Lancaster, I. I. Mazin, S. J. Blundell, P. G. Radaelli, Y. Singh, P. Gegenwart, K. R. Choi, S.-W. Cheong, P. J. Baker, C. Stock, and J. Taylor, Spin waves and revised crystal structure of honeycomb iridate Na_2IrO_3 , *Phys. Rev. Lett.* **108**, 127204 (2012).
- [14] F. Ye, S. Chi, H. Cao, B. C. Chakoumakos, J. A. Fernandez-Baca, R. Custelcean, T. F. Qi, O. B. Korneta, and G. Cao, Direct evidence of a zigzag spin-chain structure in the honeycomb lattice: A neutron and x-ray diffraction investigation of single-crystal Na_2IrO_3 , *Phys. Rev. B* **85**, 180403(R) (2012).
- [15] Y. Singh, S. Manni, J. Reuther, T. Berlijn, R. Thomale, W. Ku, S. Trebst, and P. Gegenwart, Relevance of the heisenberg-kitaev model for the honeycomb lattice iridates A_2IrO_3 , *Phys. Rev. Lett.* **108**, 127203 (2012).
- [16] S. Hwan Chun, J.-W. Kim, J. Kim, H. Zheng, C. C. Stoumpos, C. Malliakas, J. Mitchell, K. Mehlawat, Y. Singh, Y. Choi *et al.*, Direct evidence for dominant bond-directional interactions in a honeycomb lattice iridate Na_2IrO_3 , *Nat. Phys.* **11**, 462 (2015).
- [17] S. M. Winter, A. A. Tsirlin, M. Daghofer, J. van den Brink, Y. Singh, P. Gegenwart, and R. Valentí, Models and materials for generalized Kitaev magnetism, *J. Phys.: Condens. Matter* **29**, 493002 (2017).
- [18] A. Revelli, M. Moretti Sala, G. Monaco, C. Hickey, P. Becker, F. Freund, A. Jesche, P. Gegenwart, T. Eschmann, F. L. Buessen, S. Trebst, P. H. M. van Loosdrecht, J. van den Brink, and M. Grüninger, Fingerprints of kitaev physics in the magnetic excitations of honeycomb iridates, *Phys. Rev. Res.* **2**, 043094 (2020).
- [19] Y. Kim, N. Sung, J. Denlinger, and B. J. Kim, Observation of a d -wave gap in electron doped Sr_2IrO_4 , *Nat. Phys.* **12**, 37 (2016).
- [20] I. Battisti, K. Bastiaans, V. Fedeseev, A. de la Torre, N. Iliopoulos, A. Tamai, E. Hunter, R. Perry, J. Zaanen, F. Baumberger, and M. Allan, Universality of pseudogap and emergent order in lightly doped Mott insulators, *Nat. Phys.* **13**, 21 (2017).
- [21] H. Gretarsson, J. P. Clancy, X. Liu, J. P. Hill, E. Bozin, Y. Singh, S. Manni, P. Gegenwart, J. Kim, A. H. Said, D. Casa, T. Gog, M. H. Upton, H.-S. Kim, J. Yu, V. M. Katukuri, L. Hozoi, J. van den Brink, and Y.-J. Kim, Crystal-field splitting and correlation effect on the electronic structure of A_2IrO_3 , *Phys. Rev. Lett.* **110**, 076402 (2013).
- [22] R. Comin, G. Levy, B. Ludbrook, Z.-H. Zhu, C. N. Veenstra, J. A. Rosen, Y. Singh, P. Gegenwart, D. Stricker, J. N. Hancock, D. van der Marel, I. S. Elfimov, and A. Damascelli, Na_2IrO_3 as

- a novel relativistic mott insulator with a 340-meV gap, *Phys. Rev. Lett.* **109**, 266406 (2012).
- [23] C. H. Kim, H. S. Kim, H. Jeong, H. Jin, and J. Yu, Topological quantum phase transition in 5d transition metal oxide Na_2IrO_3 , *Phys. Rev. Lett.* **108**, 106401 (2012).
- [24] Y.-Z. You, I. Kimchi, and A. Vishwanath, Doping a spin-orbit Mott insulator: Topological superconductivity from the Kitaev-Heisenberg model and possible application to $(\text{Na}_2/\text{Li}_2)\text{IrO}_3$, *Phys. Rev. B* **86**, 085145 (2012).
- [25] M. Jenderka, J. Barzola-Quiquia, Z. Zhang, H. Frenzel, M. Grundmann, and M. Lorenz, Mott variable-range hopping and weak antilocalization effect in heteroepitaxial Na_2IrO_3 thin films, *Phys. Rev. B* **88**, 045111 (2013).
- [26] J. Rodriguez, G. Lopez, F. Ramirez, N. P. Breznay, R. Kealhofer, V. Nagarajan, D. Latzke, S. Wilson, N. Marrufo, P. Santiago, J. Lara, A. Diego, E. Molina, D. Rosser, H. Tavassol, A. Lanzara, J. G. Analytis, and C. Ojeda-Aristizabal, Competition between magnetic order and charge localization in Na_2IrO_3 thin crystal devices, *Phys. Rev. B* **101**, 235415 (2020).
- [27] N. Alidoust, C. Liu, S.-Y. Xu, I. Belopolski, T. Qi, M. Zeng, D. S. Sanchez, H. Zheng, G. Bian, M. Neupane, Y.-T. Liu, S. D. Wilson, H. Lin, A. Bansil, G. Cao, and M. Z. Hasan, Observation of metallic surface states in the strongly correlated Kitaev-Heisenberg candidate Na_2IrO_3 , *Phys. Rev. B* **93**, 245132 (2016).
- [28] L. Moreschini, I. Lo Vecchio, N. P. Breznay, S. Moser, S. Ulstrup, R. Koch, J. Wirjo, C. Jozwiak, K. S. Kim, E. Rotenberg, A. Bostwick, J. G. Analytis, and A. Lanzara, Quasiparticles and charge transfer at the two surfaces of the honeycomb iridate Na_2IrO_3 , *Phys. Rev. B* **96**, 161116(R) (2017).
- [29] F. Lüpke, S. Manni, S. C. Erwin, I. I. Mazin, P. Gegenwart, and M. Wenderoth, Highly unconventional surface reconstruction of Na_2IrO_3 with persistent energy gap, *Phys. Rev. B* **91**, 041405(R) (2015).
- [30] T. E. Dziuba, Combined study of local spectroscopy and macroscopic electronic transport of the correlated honeycomb spin-orbit Mott insulator Na_2IrO_3 , Dissertation, Georg-August-Universität Göttingen, 2021.
- [31] K. Mehawat and Y. Singh, First-order density-wave-like transitions in surface-doped Na_2IrO_3 , *Phys. Rev. B* **94**, 041109(R) (2016).
- [32] A. S. Moskvina, J. Málek, M. Knupfer, R. Neudert, J. Fink, R. Hayn, S.-L. Drechsler, N. Motoyama, H. Eisaki, and S. Uchida, Evidence for two types of low-energy charge transfer excitations in Sr_2CuO_3 , *Phys. Rev. Lett.* **91**, 037001 (2003).
- [33] R. Deslattes, E. Kessler, Jr., O. Indelicato, and E. Lindroth, *International Tables for Crystallography* (Wiley Online Library, Weinheim, Berlin, 2006), Vol. C, Chap. 4.2, pp. 200–212.
- [34] F. Freund, S. C. Williams, R. D. Johnson, R. Coldea, P. Gegenwart, and A. Jesche, Single crystal growth from separated educts and its application to lithium transition-metal oxides, *Sci. Rep.* **6**, 35362 (2016).
- [35] S. Manni, S. Choi, I. I. Mazin, R. Coldea, M. Altmeyer, H. O. Jeschke, R. Valentí, and P. Gegenwart, Effect of isoelectronic doping on the honeycomb-lattice iridate A_2IrO_3 , *Phys. Rev. B* **89**, 245113 (2014).
- [36] R. Castaing, Electron probe microanalysis, *Adv. Electron. Electron Phys.* **13**, 317 (1960).
- [37] P. J. Moll, Focused ion beam microstructuring of quantum matter, *Annu. Rev. Condens. Matter Phys.* **9**, 147 (2018).
- [38] J. Krizan, J. Roudebush, G. Fox, and R. Cava, The chemical instability of Na_2IrO_3 in air, *Mater.* **52**, 162 (2014).
- [39] N. W. Ashcroft and N. D. Mermin, *Solid State Physics* (Saunders College Publishing, New York, 1976).
- [40] Y. Maeno, K. Yoshida, H. Hashimoto, S. Nishizaki, S.-i. Ikeda, M. Nohara, T. Fujita, A. P. Mackenzie, N. E. Hussey, J. G. Bednorz, and F. Lichtenberg, Two-dimensional Fermi liquid behavior of the superconductor Sr_2RuO_4 , *J. Phys. Soc. Jpn.* **66**, 1405 (1997).
- [41] J. Seidel, L. W. Martin, Q. He, Q. Zhan, Y.-H. Chu, A. Rother, M. Hawkrige, P. Maksymovych, P. Yu, M. Gajek *et al.*, Conduction at domain walls in oxide multiferroics, *Nat. Mater.* **8**, 229 (2009).
- [42] P. Maksymovych, J. Seidel, Y. H. Chu, P. Wu, A. P. Baddorf, L.-Q. Chen, S. V. Kalinin, and R. Ramesh, Dynamic conductivity of ferroelectric domain walls in BiFeO_3 , *Nano Lett.* **11**, 1906 (2011).
- [43] S. Ghara, K. Geirhos, L. Kuerten, P. Lunkenheimer, V. Tsurkan, M. Fiebig, and I. Kézsmárki, Giant conductivity of mobile non-oxide domain walls, *Nat. Commun.* **12**, 3975 (2021).